Geodetic evidence for *en echelon* dike emplacement and concurrent slow-slip at Kilauea volcano, Hawaii,17 June 2007.

E.K. Montgomery-Brown,[1] D.K. Sinnett,[1] M. Poland,[2] P. Segall,[1] T. Orr,[2] H. Zebker,[1] A. Miklius,[2]

E. K. Montgomery-Brown, Department of Geophysics, Stanford University, Stanford, CA, 94305, USA. (emilyd@stanford.edu)

D. K. Sinnett, Department of Geophysics, Stanford University Mitchell Building, Stanford, CA 94305, USA.(dsinnett@stanford.edu)

M. Poland, USGS, Hawaii Volcano Observatory, Hawaii National Park, HI, 86718, USA

T. Orr, USGS, Hawaii Volcano Observatory, Hawaii National Park, HI, 86718, USA

P. Segall, Department of Geophysics, Stanford University, Stanford, CA, 94305, USA

H. Zebker, Department of Geophysics, Stanford University, Stanford, CA, 94305

A. Miklius, USGS, Hawaii Volcano Observatory, Hawaii National Park, HI, 86718, USA

[1]Department of Geophysics, Stanford University, Stanford, CA, 94305, USA.

[2] U.S.G.S., Hawaiian Volcano Observatory, Hawaii National Park, HI 96718 United States

Abstract. An intrusion at Kīlauea Volcano, Hawaii, 17 June – 19 June 2007, began with an intrusion in the upper east rift zone (ERZ) and culminated with a small eruption (1500 m^3). Surface deformation due to the intrusion was recorded in unprecedented detail by Global Positioning System (GPS) and tilt networks as well as Interferometric Synthetic Aperture Radar (InSAR) data acquired by the ENVISAT and ALOS satellites. A joint nonlinear inversion of GPS, tilt, and InSAR data yields a deflationary source beneath the summit caldera and an ENE-striking uniform-opening dislocation with $\sim$2 m opening, a dip of $\sim 80^o$ to the south, and extending from the surface to $\sim$2 km depth. This simple model reasonably fits the overall pattern of deformation but significantly misfits data near the western end of the dike. Three more complex dike models are tested that allow for distributed opening including: 1) a dike that follows the surface trace of the active rift zone, 2) a dike that follows the axis of InSAR deformation, and 3) two *en echelon* dike segments beneath mapped surface cracks and newly-formed steaming areas. The *en echelon* dike model best fits local GPS and tilt data. Maximum opening occurred on the eastern segment beneath the eruptive vent. Although this model is the best fit to the ERZ data, it fails to explain data from a coastal tiltmeter and GPS sites on Kīlauea's southwestern flank, which exhibit displacements consistent with previous slow-slip events beneath Kīlauea's south flank. Tilt at the coastal tiltmeter is also consistent with predictions based on previous slow-slip events but inconsistent with intrusion-only models. An inversion including slip on a basal décollement improves fit to these

data and suggests ∼15 cm of fault motion, comparable to previous slow-slip events.

1. Introduction

An intrusion in Kīlauea Volcano's east rift zone (Fig. 1) began in the early morning of June 17, 2007, Hawaiian Standard Time (HST=UTC-10). This event, the fourth in a series of small intrusions [*Heliker and Mattox*, 2003] since the installation of continuous GPS at Kīlauea in 1996, was observed in unprecedented detail by GPS, tiltmeters, and interferometric synthetic aperture radar (InSAR). The intrusion culminated in the eruption of ∼1500 m^3 of lava from a vent near Makaopuhi Crater (∼6 km west of Puʻu ʻŌʻō and ∼13 km southeast of the summit) on June 19. Although small in erupted volume, the event significantly disrupted the magmatic plumbing system, and led to ∼80 m of crater floor subsidence at Puʻu ʻŌʻō and a temporary cessation of eruptive activity there [*Poland et al.*, 2008]. Eruptive activity resumed at Puʻu ʻŌʻō on July 1. For simplicity, we refer to this event as the intrusion throughout the paper.

In addition to the magmatic events, far field GPS and tiltmeter measurements suggest concurrent south flank deformation [*Brooks et al.*, 2008; *Montgomery-Brown et al.*, 2007] similar to previously observed slow-slip events [*Cervelli et al.*, 2002b; *Brooks et al.*, 2006; *Segall et al.*, 2006]. In this paper we test a spectrum of different models of the event, including magma chamber deflation and dike opening, as well as slip on a possible décollement beneath Kīlauea, to better constrain the deformation sources.

1.1. Geologic Setting

The major structural features of Kīlauea include a summit caldera and two radial rift zones extending to the southwest (SWRZ) and east (ERZ) (Fig. 1). Deformation at the summit caldera can be characterized by inflation and deflation cycles associated with a shallow magma chamber [*Dvorak and Dzurisin*, 1997]. With the exception of three brief inflationary periods associated with changes in vent geometry at Puʻu ʻŌʻō, the summit subsided continuously between 1983 and 2003, after which it began uplifting [*Miklius*, 2005; *Poland et al.*, 2008]. The ERZ undergoes persistent extension due to intermittent magmatic events and southward motion of the volcano's south flank [*Owen et al.*, 2000a]. Motion of the south flank is likely accommodated by slip along a basal décollement, interpreted as the interface between sea floor sediments and the overlying volcanic pile [e.g., *Nakamura*, 1980; *Got and Okubo*, 2003; *Morgan and McGovern*, 2003]. Quasi steady-state deformation during the 1990's is well modeled by summit deflation, 20-30 cm/yr of slip on the décollement, 20 cm/yr of opening in the deep (below ∼2 km) ERZ, and 12 cm/yr of left-lateral strike-slip in the upper ERZ [*Owen et al.*, 2000a].

Recent upper ERZ intrusions (e.g. January 1997, *Owen et al.* [2000b] and September 1999, *Cervelli et al.* [2002a]) manifested as swarms of shallow seismicity accompanied by rapid rift extension and summit subsidence. *Owen et al.* [2000b] and *Cervelli et al.* [2002a] found that geodetic data associated with these intrusions can be fit by shallow (bottom depth <2.5 km), steeply southward-dipping dikes. These events were associated with cessation of eruptions at Puʻu ʻŌʻō for 24 and 11 days respectively—the longest such pauses in the Puʻu ʻŌʻō - Kupaianaha eruption since the beginning of continuous effusion in 1986 [*Heliker and Mattox*, 2003]. A third intrusion, for which geodetic data have not been modeled, occurred in 2000 [*Heliker and Mattox*, 2003; *Miklius et al.*, 2005].

The south flank also hosts aseismic slip events, first noted by *Cervelli et al.* [2002b]. Since then a total of 8 slow-slip events have been identified between 1998 and 2007; the most recent prior to 2007 occurred in January 2005 [*Brooks et al.*, 2006; *Segall et al.*, 2006].

Past slow-slip events released equivalent strain to regular earthquakes ranging from M_w 5 to M_w 6 over the course of 36-48 hours [*Montgomery-Brown et al.*, 2009]. The four most similar slow-slip events appear to exhibit a 2.1 yr periodicity [*Brooks et al.*, 2006]. At the time, this observation led to the anticipation of an event in March 2007 and prompted the joint deployment of additional seismic instruments, two south flank tiltmeters, and an augmented GPS array in early 2007 by the University of Hawai'i, University of Wisconsin, the Hawaiian Volcano Observatory (HVO), and Stanford University.

1.2. Event Chronology

The June 2007 intrusion occurred in four distinct pulses (Fig. 2, times A, B, C, D) distinguished in the seismic and geodetic records [*Wilson et al.*, 2007; *Poland et al.*, 2008]. The intrusion began on June 17, 12:16 UTC (A in Fig.2) with an earthquake swarm centered 1.5-2 km southwest of Mauna Ulu. More than 38 earthquakes with M >2 occurred during the first 2 hours of the swarm [*Wilson et al.*, 2007]. Summit deflation and southward tilt at ERZ site ESC began simultaneously with the increase in seismicity, followed minutes later by tilt changes at Pu'u 'Ō'ō. Over the next 5.5 hours, the tiltmeter ESC in the ERZ (Fig. 2) accumulated $\sim$70 μrad of southward tilt. Seismicity then concentrated down-rift coinciding with an increase in summit tilt rates (17:40 UTC, B in Fig. 2), the onset of rift zone extension between GPS stations KTPM and NUPM (which span the ERZ near Makaopuhi crater), and slowing of tilt at ESC.

Seismicity propagated down-rift between June 17 19:00 (C in Fig. 2) and June 19 01:15 UTC (D in Fig. 2), although seismicity rates had slowed to 3 locatable events per hour after June 17 24:00. During this time, the tiltmeter at Pu'u 'Ō'ō (tiltmeter POC) recorded steady tilt toward the crater. The summit and Pu'u 'Ō'ō continued to subside at a diminishing rate up to June 19 01:15 (D in Fig. 2) when summit and Puʻu ʻŌʻō tilt rates increased slightly coinciding with the final down-rift concentration of seismicity. The same pattern is observed in the baseline length between KTPM and NUPM. Summit subsidence and rift zone extension continued at diminishing rates until June 19 20:30 (E in Fig. 2), when the summit returned to inflation. Tiltmeter POC continued to record deflation at Puʻu ʻŌʻō, however, until June 27.

Cracks developed at multiple locations in the ERZ, and steam vents formed along the western base and slope of Kāne Nui o Hamo. At the eastern end of the cracked zone, a small amount of fresh lava was observed on the north flank of Kāne Nui o Hamo by geologists from the Hawaiian Volcano Observatory on the morning of June 19. At Puʻu ʻŌʻō, a lack of lava at the surface by June 19 indicated a pause in the eruption that lasted until July 2. The pause was likely caused by the interruption of the magma supply to the vent.

2. Data

The Hawaiian Volcano Observatory (HVO), in conjunction with Stanford University and the Pacific GPS Facility University of Hawaii, operate an array of continuous GPS stations on Kīlauea vVolcano. The tiltmeter network on Kīlauea is also operated by HVO, with two new sites installed in anticipation of an early 2007 slow-slip event. The tilt and GPS instruments provide detailed temporal information on magmatic and tectonic deformation at Kīlauea but are spatially sparse. Temporally sparse, but spatially dense, coverage of deformation is provided by InSAR data from multiple satellites. All data sets have been transformed into a local cartesian coordinate system with an origin at GPS site MANE (-155.273, 19.339). We analyze these various data sets sets together: three components of displacement from 40 GPS sites, line of site (LOS) displacements from three InSAR images, and two perpendicular components of tilt from nine tiltmeters.

2.1. GPS

Daily GPS solutions are computed at HVO using the GIPSY/OASIS II software package developed at the Jet Propulsion Laboratory (JPL) in precise point positioning mode with non-fiducial orbits [*Gregorius*, 1996; *Zumberge et al.*, 1997]. The daily non-fiducial solutions are transformed into a global ITRF2005 reference frame [*Altamimi et al.*, 2007] with a 7 parameter Helmert transformation provided by JPL. Since the GPS solutions are tightly constrained in GIPSY, the output formal errors are unrealistically small (10^{-5} - 10^{-6} m). We therefore scale the output covariance matrices by 10^3 which retains the relative error information but makes the diagonal elements of the covariance the same order of magnitude as the average standard deviations of the time series (E - 0.003 m, N - 0.002 m, U - 0.015 m, computed from two weeks of data during a geodetically quiet period).

Outliers, daily reference frame realization errors, and average velocities are regularly estimated from the entire available set of GPS data from HVO. Outliers, defined as any daily position that is more than 10 cm higher or lower than the mean of that station's position for a five day window, are removed from the continuous time series. This outlier filtering removes only a few days from the six months of continuous GPS data included in this study. An estimated velocity of the Mauna Kea permanent GPS station is also subtracted from all stations to put the displacements in a local (island-fixed) reference frame.

We then use a Kalman filter to estimate and remove an average velocity and daily errors in the reference frame realization using a variation of the observation equation proposed by *Miyazaki et al.* [2003]:

$$\mathbf{X}(t) = \mathbf{X_o} + L(\mathbf{x}, t - t_o) + \mathbf{v}(t - t_o) + F\mathbf{f}(t) + \epsilon, \quad (1)$$

where $\mathbf{X}$ is the daily position of each station, $\mathbf{X_o}$ is initial station position at time t_o, L is a random walk process accounting for local benchmark wobble, $\mathbf{v}$ is a constant station velocity, F is a Helmert transformation, $\mathbf{f}$ is a vector of frame translations and rotations which are modeled as a white noise process, and ϵ is the remaining error. At several points in the time series, steps occur due to geologic (e.g., the current intrusion) or man-made (e.g., equipment changes) events. At these times, we reset the variance of L to a large value, allowing the offsets to occur without influencing the velocity or reference frame terms. The average velocity of each site and reference frame errors estimated by the Kalman filter are then subtracted from the time series.

In June 2007, the Kīlauea GPS network included 16 continuous and 14 campaign stations that were measured before and after the intrusion (Fig. 3). Continuous GPS data between January 1, 2007 and July 1, 2007 are used to compute displacements during the intrusion. Most of the campaign measurements spanning the intrusion contain little secular deformation, since the 2007 Kīlauea GPS campaign had just been completed at the time of the intrusion. HVO staff were able to quickly re-occupy many sites in the days immediately following the intrusion. Campaign data between 2002 and 2007 are used, with data before 2007 used to constrain site velocities at sites not measured immediately before the June 17 intrusion.

We invert for the GPS displacements spanning the intrusion using a least squares algorithm. Estimated parameters include the pre-intrusion station position $\mathbf{X_o}$, any residual deviations from the previously computed average velocity, $\mathbf{v}t$, and the co-eruptive displacements. Residual velocities are usually very small (<1 cm/yr). Data from June 16-20, 2007, while the intrusion was in progress, are removed in this analysis, as we estimate only the cumulative deformation. The displacement is modeled as a Heaviside function, H, scaled by $\mathbf{d}$, the magnitude of the displacement vector on June 20, 2007:

$$\mathbf{X} = \mathbf{X_o} + \mathbf{v}t + \mathbf{d}H(t_{Jun20}). \tag{2}$$

The displacements, $\mathbf{d}$, are analyzed in this study and shown in map view in Figure 3. Several major features of the event are readily apparent in the GPS displacements. First, extension across the ERZ is obvious, particularly the ∼0.9 m separation between stations KTPM and NUPM. Second, the summit-area GPS sites displace inward, suggesting summit subsidence. Third, a large signal is seen at PUOC associated with collapse of the Pu‘u ‘Ō‘ō cone.

2.2. Tilt

HVO operates a network of electronic borehole tiltmeters around the summit, along the ERZ, and on the south flank (Fig. 4). We use data only from tiltmeters that have demonstrated good ground coupling. Because the instruments are emplaced at shallow depths, nearly every tiltmeter exhibits strong diurnal tilts. The magnitude and structure of the diurnal variations depend on local installation conditions.

Tiltmeters are installed in boreholes ∼3 m deep and covered, though not sealed, at the surface. The tiltmeter installations record two components of tilt, surface temperature, down-hole temperature, and rainfall once per minute. No rainfall was recorded during the intrusion, simplifying the interpretation of the data.

Daily variations in tilt depend on temperature variations and solid earth tides. Local geology at the site determines the response at each station to temperature and tidal forces. To better discern the magnitude of tilt offsets during the intrusion, we tested several different methods of filtering the diurnal variations before selecting a notch filter as the optimal method.

The filter was designed as a time domain filter with a frequency domain specification. We first removed diurnal periods of 24$\pm$3.6 hours, which revealed semi-diurnal tidal variations; these were subsequently removed with a notch at 12$\pm$3.6 hours, resulting in a smooth signal. An example of the pre- and post-filtered tilt series for station KAE is shown in Figure 5.

Cumulative tilts analyzed in the inversions are determined by differencing the three day pre-event (June 10 - 13) average from the three day post-event (June 22 - 25) average. The same time period for each station is used to calculate standard deviations from the means for tilt sites. Several features are immediately obvious in the tilts (Fig. 4). Largely inward tilt at the summit indicates caldera subsidence. A large tilt signal is also observed at ESC ($\sim$80 μrad of SSW tilt). Near Puʻu ʻŌʻō, PUO and POO both tilt toward the collapsed cone. Lastly, a small, but notable, northwestward tilt occurred at the coastal tiltmeter KAE.

2.3. InSAR

Radar interferograms constructed from data acquired by the ENVISAT ASAR and ALOS PALSAR instruments provide excellent spatial resolution of the deformation field associated with the June 17-19, 2007 intrusion and eruption at Kīlauea. An ascending ENVISAT interferogram (Fig. 6, a) (12 April - 22 June, 2007) and an ascending ALOS interferogram (Fig. 6, b) (5 May - 20 June 2007) span the intrusion and eruption. GPS results suggest little deformation between 12 April and the onset of intrusive activity on 17 June; therefore, the displacements in the interferograms can be almost totally ascribed to the 17-19 June intrusive and eruptive activity. The ENVISAT radar operates at C-band (5.6 cm wavelength), which does not penetrate vegetation well, and leads to decorrelation in the rainforest north of the ERZ. The ALOS PALSAR has an L-band radar (23 cm wavelength), which better penetrates vegetation, resulting in improved coherence north of the ERZ. An additional descending ALOS interferogram (28 November 2006 - 16 July 2007) is also used in the inversions, although we remove the summit area from our analysis due to uplift suggested in the GPS data in the month following the intrusion (Fig. 6, c).

Subsequent spatial averaging of the interferograms using a quadtree algorithm reduces the size of the data vector and LOS errors in a statistical sense, but does not reduce any systematic biases. The covariance structure of InSAR measurements, which depends on atmospheric delays, uncompensated topography, and orbit errors, is difficult to model; therefore, we use a diagonal covariance matrix with variances calculated for each quadtree box within the quadtree algorithm [*Welstead*, 1999].

Displacements in the ascending interferograms include LOS lengthening (subsidence) centered near Halemaumau Crater in Kīlauea's caldera, as well as two lobes of LOS shortening (uplift), with LOS lengthening in the center along the ERZ near Makaopuhi Crater (Fig. 6, b). The descending image is dominated by LOS shortening (upward and southward motion) on the south side of the ERZ (Fig. 6, c).

2.4. Ground cracks and lava flow

After the eruptive episode, cracks in the east rift zone above the presumed intrusion were mapped on foot by geologists from the Hawaiian Volcano Observatory (Fig. 7). The main crack system associated with the intrusion was mapped on June 18, 2007, but subsequent visits to the area after the intrusion found additional cracking. Most cracks occur in a zone ∼600 m wide and are oriented ∼65^o as measured by Brunton compass. Both right- and left-stepping cracks were mapped. The crack zone extends down-rift over a distance of 3 km, beginning 1.3 km east of the summit of Mauna Ulu, crossing the north flank of Kāne Nui o Hamo, and extending as far as the eruption site. The western end of the cracked area was examined in more detail, confirming its broad, blunt character. No cracks were observed east of the eruption site.

The area east of Pauahi Crater, along the Nāpau hiking trail, also hosted some cracks oriented 65^o, although this zone was much less well developed than the main crack zone to the east. A series of larger, *en echelon* cracks in this zone cut the Mauna Ulu road and even defined a low hump crossing the pavement (Fig. 7).

A final cluster of cracks mapped on the Chain of Craters road were also directly related to the June 2007 event, extending a few hundred meters to either side of the highway (Fig. 7). The crack orientations ranged from 90^o to 115^o and appeared to trend westward into a north-facing normal fault in the Koaʻe fault zone that is buried by a 1969 lava flow. Slip on this fault occurred during the September 1999 intrusion [*Cervelli et al.*, 2002a]. The largest of the new cracks in this zone had 2 cm of separation, with a suggestion of south-side-up motion. Measurements of the distance between pins spanning a 5-10 m wide crack at crack station 98-10 (Fig. 7) indicate 3.9±0.4 cm of opening between April 30, 2003 and July 12, 2007. Opening at crack station 98-11 was within errors at 0.2±0.4 cm during the same time period. Although this is a long time interval, past measurements at this site have shown little movement except during intrusions, suggesting that much of this measured opening could be attributed to the June 2007 intrusion (D. Swanson, pers. comm. April 2009). A campaign GPS site (69FL) and a discontinuity in the ascending ALOS interferogram (Fig. 6, b) are located nearby and may be affected by this ground cracking. Effects of this normal faulting on the inversions are presented following discussion of the models.

3. Model Inversions

Observed GPS displacement and tilt patterns are similar to previous dike intrusions on Kīlauea [*Owen et al.*, 2000b; *Cervelli et al.*, 2002a]. We therefore begin with a simple model of the event consisting of a Mogi source of volume change [*Mogi*, 1958] and a rectangular dislocation with uniform opening [e.g., *Okada*, 1985] in an isotropic, homogeneous, linearly elastic half space to model summit deflation and ERZ opening respectively.

3.1. Optimal Uniform Opening Dike

To determine constraints on the distributions of possible source parameters, we employ Markov Chain Monte Carlo (MCMC) optimization [*Metropolis et al.*, 1953] to build posterior distributions of the parameters describing an inflating planar dislocation in the rift zone (length, width, depth, dip, strike, east position, north position, and opening) and a deflating Mogi source at the summit (east position, north position, depth, and volume change). The *a priori* distribution of model parameters is assumed to be uniform between broadly chosen bounds. Since lava was erupted at the surface, we constrain the top of the dike to lie within half a kilometer of the surface. We also apply a maximum excess-dike pressure constraint, which discourages models with unrealistic aspect ratios. We use the optimum model from a short MCMC search (1 million samples) to initiate a thorough search of 10 million samples of the model space. We save every 10th model to avoid correlation between model steps [*Fukuda and Johnson*, 2008].

The optimal uniform opening dike is sub-vertical (dipping 81^o to the south), $\sim$4 km in length, and extends from the surface to a depth of $\sim$2 km, with $\sim$1.9 m of opening. The modeled dike strikes along observed surface disruptions (the eruption site, ground cracks, and steaming areas) and follows the linear part of the axis of deformation seen in both the ascending ALOS and ENVISAT interferograms (Fig. 8). To first order, this model fits the observed GPS displacements, InSAR LOS displacements, and tilt. Despite the overall fit, however, there are several obvious misfits (Fig. 8). Predicted tilt at ESC is roughly 90^o from observed. Predicted displacements at 69FL are in the opposite direction from the observed, and far smaller in magnitude; this misfit may be a result of motion along the Koa'e fault system near station 69FL. In addition, predicted displacements at MULU and GOPM are far smaller in magnitude than observed. The summit area GPS sites are also not well fit by this model; predicted displacements show a systematic westward misfit.

Single dislocation models of the dike, while simplistic, do allow us to constrain the range of possible parameters that fit the data. Certain parameters are well constrained, such as the position and length of the dike, which are limited by the down-rift extent of deformation recorded by InSAR, and the westward displacements at campaign GPS sites KANE and PKMN. Somewhat less well constrained are the strike, dip and amount of opening. Ninety-five percent of the models have strikes that range from $55 - 80^o$, while acceptable dips can range from about $70 - 107^o$ to the south (Fig. 9). The amount of opening ranges from ∼1.3 to 7.8 m, and is correlated with the size of the dike (i.e., smaller dikes have more opening), such that dike volume is well-constrained (Fig. 9). While useful in constraining dike parameters in a statistical sense, these overly-simplistic models are unable to sufficiently fit near-field data. We thus turn to distributed opening models.

3.2. Distributed Opening Dike Models

Three different dike geometries are tested in linear, distributed opening inversions. Mogi sources are also included under the summit and Pu'u 'Ō'ō at depths of 2.5 km and 100 m respectively. The summit source depth was determined from the MCMC inversions, while the source beneath Pu'u 'Ō'ō was chosen to be consistent with the depth of open-system degassing [*Edmonds and Gerlach*, 2007]. The three different dike models (Fig. 10) are based on particular geologic and geodetic observations and are constructed from uniform opening rectangular patches ∼0.5 km on each side. Noting that the earthquakes associated with this intrusion follow the curve of the east rift zone, we construct the first model, Curving Dike (1), following the surface trace of the recently active part of the rift zone marked by spatter cones and pit craters (Fig. 1). We construct a second model, Curving Dike (2), following the axis of deformation in the ascending ALOS interferogram, which does not follow the surface trace of the rift zone, but instead continues to trend westward after the rift zone curves north toward the summit (Fig. 6). The third model (3) is a pair of *en echelon* dikes aligned with mapped areas of surface cracking (Fig. 7). *En echelon* dikes and fissures are commonly observed during rift zone eruptions; examples can be found in Iceland [e.g., *Gudmundsson*, 2003] and in previous eruptions of Kīlauea [e.g., *Fiske and Koyanagi*, 1968]. A small right step (∼100 m) in the crack zone was also observed near the small pad of lava at Kāne Nui o Hamo at the far eastern end cracked zone. Because geodetic data are unable to resolve such a small separation, and the InSAR images decorrelate over the dike, none of the models address this level of detail.

The distributed opening inversions are accomplished with a non-negative least squares algorithm that minimizes the L2-norm of the weighted residuals. Spatial smoothing is applied with a Laplacian operator for each dike segment, with one smoothing parameter each for both curving dike models, and two for the *en echelon* model (one for each dike). A line search for the optimal smoothing parameter is conducted (grid search of two smoothing parameters in the case of the *en echelon* dikes), and the optimal weight chosen with the L-curve criteria [*Hansen*, 1992] such that the optimal parameter produces the smoothest model with a minimal increase of the residual norm (Fig. 11).

The opening distribution shown in Figure 12 is representative of all three distributed opening models, with a maximum of $\sim$2 m of opening between Makaopuhi and Nāpau Craters. A second local maximum opening of nearly 2 m occurs near Pauahi Crater. The majority of the modeled opening is concentrated beneath the mapped areas of surface cracking, and opening tapers sharply to zero down-rift of the small pad of lava on Kāne Nui O Hamo (Fig. 12).

We use the percentage of data variance (1-$||d - \hat{d}||/||d||$, where d is the data vector, and $\hat{d}$ is the model prediction) explained by the model as a measure of misfit. The total percentage of data variance explained by the distributed opening models ranges from 44 to 89%, but individual subsets of the data are better fit than others (Tab. 1). Particular models, however, also have disqualifying features. Both the model that follows the rift zone and the model that follows the axis of InSAR deformation are unable to reproduce the $\sim 110^o$ difference in the GPS (PULU) and tilt (ESC) directions at the west end of the dike. In fact, neither curving dike produces southward tilts at ESC; both predict northwest tilt. The *en echelon* model, while not perfectly fitting these two stations, provides a much better fit than either of the curving dike models (Fig. 13).

We note that the western *en echelon* segment is very near the September 1999 dike, but strikes 67^o as opposed to 85^o [*Cervelli et al.*, 2002a]. We tested models with the western dike segment striking 85^o as in the 1999 intrusion. The overall percentage of variance fit by this model, and the percentage of the InSAR variance fit locally near Pauahi Crater are the same as those for the parallel *en echelon* segments. The 67^o strike is preferred here because it is consistent with the orientation of the cracks observed along the Nāpau trail, and is able to model the $\sim 110^o$ difference in the co-located sites ESC (tilt) and PULU (GPS). The 85^o striking dike model is unable to produce the observed northwestward displacement direction at PULU.

As noted in Section 2.4, it is possible that slip may have occurred on a north-dipping normal fault in the Koa'e fault zone, as was the case during the 1999 intrusion [*Cervelli et al.*, 2002a]. This hypothesis is supported by the offset seen in the ascending ALOS interferogram near site 69FL (Fig. 13) and by cracks observed along Chain of Craters road (Fig. 7). To test how the data near the crack zone may have influenced our inversions, we remove GPS site 69FL and InSAR pixels in a 2 km by 1 km box around the Chain of Craters road cracks, and re-invert for the distributed dike opening. Overall percentages of the data variance fit by the models remain the same, but a small volume increase and ~ 1 km eastward shift of the maximum opening on the western dike segment predict tilts at

ESC that are $\sim 30^o$ westward of the observed. The predicted tilt at ESC is still southward and close to the observed magnitude, which neither of the curving dikes can produce.

If we include a steeply north-dipping normal fault at the location of cracks and InSAR phase discontinuity extending from the surface to 1 km deep, inversions estimate $\sim$10 cm of slip on the normal fault. This amount of slip does not significantly influence the predicted tilt at ESC, since it only contributes $\sim$1 μrad while the total observed tilt at ESC was $\sim$80 μrad. A normal fault that breaks the surface has a very sharp displacement discontinuity, and is too sharp to reproduce the gradient observed in a N-S profile of the InSAR data through the center of the normal fault. Deepening the top of the fault to 50 m below the surface increases the amount of estimated slip to $\sim$20 cm and provides a better fit to the InSAR profile immediately above the normal fault.

Despite including a normal fault, dike opening on the western segment is still required to fit the the magnitude of the uplift observed in the InSAR to the north and south of the fault, and the GPS displacements at PULU and 69FL. The presence of the normal fault in the models shifts the optimal location of maximum dike opening on the western segment about 1 km eastward, similar to models where data near the crack zone were removed. Based on this inversion, which included a normal fault, and the previous one, which removed data near the normal fault, the preference for the overall dike model of two *en echelon* segments does not change. It is likely, however, that a pre-existing normal fault in the Koa‘e fault system above the western segment slipped during the intrusion.

While the *en echelon* dike model is the best fit to the near-field observations, there are some notable local misfits to all of the dike models: 1) the direction and magnitude of the southwestern flank GPS stations (PGF1, PGF5 and PGF6) (also noted by *Brooks et al.*

[2008]), 2) opposite sign of tilt at coastal site KAE, and 3) over-prediction of GPS sites north of the east rift zone. These particular misfits, further detailed in the next section, lead us to believe that a dike-only model may not be sufficient to model these data.

3.3. Evidence for concurrent slow-slip

The tiltmeter KAE, installed at the coast in early 2007 to record an anticipated slow-slip event [*Brooks et al.*, 2006], tilted down to the north during the June 2007 intrusive event. Models of typical east rift zone intrusions predict southward tilts at the coast. Tilts predicted by models of the 2005 slow-slip event model [*Segall et al.*, 2006], however, do tilt to the north. During the intrusion, vertical displacements at coastal GPS sites are consistent with the tilt, exhibiting subsidence along the coast, while similarly distant GPS sites to the north of the rift do not. Models of dikes that break the surface would produce uplift everywhere, which is inconsistent with the data. Offshore décollement slip, however, produces subsidence on the south flank and northward tilting, as observed (Fig. 14, insets).

The displacements in the far western part of the Kīlauea GPS network are consistent with those measured during previous slow-slip events [*Brooks et al.*, 2008]. None of the intrusions previously observed by continuous GPS (e.g., 1997, 1999 and 2000) produced significant deformation at these sites, nor do any of the dike-only models discussed as part of this study. In addition, previous slow-slip events are associated with a distinct pattern of microearthquakes [*Segall et al.*, 2006; *Wolfe et al.*, 2007]. A similar cluster of microearthquakes was observed during the 2007 intrusion, but not during the 1997 and 1999 intrusions [*Brooks et al.*, 2008]. Although the slouth flank earthquake swarm is suggestive, the south flank is known to be highly active following rift zone intrusions [*Dvorak* *et al.*, 1986], and this particular cluster of earthquakes is often active without an apparent trigger [*Montgomery-Brown et al.*, 2009]. Nevertheless, together these observations compel us to test models including dike opening and décollement slip.

3.4. Dike Intrusion and Décollement Slip

Here we examine inversions that include slip on a décollement structure beneath Kīlauea's south flank in addition to the same dike-only models presented in Section 3.2. The sub-horizontal décollement is located at a depth of 8 km coinciding with the planar alignment of décollement earthquakes [*Got and Okubo*, 2003; *Hansen et al.*, 2004] and the inferred depth of the slow-slip events [*Segall et al.*, 2006; *Montgomery-Brown et al.*, 2009]. For our models, the décollement plane is divided into a twenty-by-twenty grid of fault patches 2 km square. A Laplacian smoothing operator is applied to the dislocation models of the décollement as well as the dikes, and the weights are again determined by the L-curve criteria.

While including the décollement produces minor differences in the dike opening distribution, the major features remain the same with the majority of the opening occurring under the mapped surface cracks. The total estimated dike volume is 16.6 x 10^6 m^3 (western segment: 0.79 x 10^6 m^3, eastern segment: 15.8 x 10^6 m^3). The summit's volume loss is 1.8 x 10^6 m^3, while Pu'u 'Ō'ō's volume loss is 0.02 x 10^6 m^3.

As in the 1997 [*Owen et al.*, 2000b] and 1999 [*Cervelli et al.*, 2002a] intrusions, volume loss from the summit does not account for volume gain from the dike. The pair of *en echelon* dikes constitute a total volume increase of 1.66×10^7 m^3, while deflation at the summit and Pu'u 'Ō'ō magma chambers account for a total volume loss 1.82×10^6 m^3. We can estimate the volume of magma drained from the cone of Pu'u 'Ō'ō from the length of time it took for lava to re-appear at Puʻu ʻŌʻō (12 days) and the magma supply rate to Kīlauea. During the first twenty years of eruption the magma supply rate was 0.12 km^3/yr [*Heliker and Mattox*, 2003], which is probably a minimum since *Poland et al.* [2008] suggested the magma supply rate had increased between 2003 and 2006. This minimum rate implies that at least $3.65 \times 10^6 m^3$ of lava drained from Puʻu ʻŌʻō, giving a ratio of dike volume gain to magma chamber loss, r_v, of 3.03.

Deeper, geodetically undetectable sources are often called upon to explain volume discrepancies. On Kīlauea, the deep rift zone may be one such source. *Rivalta and Segall* [2008], however, showed that this difference may also be explained by the compressibility of the magma, and the shapes of the magma chambers, and dikes. *Rivalta and Segall* [2008] found ratios of dike volume gain to magma chamber loss, r_v, range between 1.24 and 4.33 based on realistic values of magma compressibility and rock rigidity for Kīlauea volcano, consistent with the values estimated above for the June 2007 event.

Regardless of the details of the dike geometry, maximum seaward décollement slip estimates are $\sim$15 cm with a moment magnitude of M_w=5.7. While the magnitude and location of this event are similar to previous slow-slip events, the number of south flank aftershocks is far fewer than similarly sized slow-slip events that occurred in the absence of intrusions [*Montgomery-Brown et al.*, 2009]. Slip is concentrated south of the Hilina fault system and close to the coast, as was seen in previous slow-slip events [*Montgomery-Brown et al.*, 2009].

In general, models including slip on the décollement result in misfits similar to dike-only models. The total percentage of the data variance explained by models that include the décollement shows slight improvements relative to the dike-only models, but we have also increased the number of free model parameters. Independently, the GPS and InSAR data are each better fit by a few percent (Tab. 1). As in dike-only models, the *en echelon* segments are a significantly better fit for the InSAR data.

The fits to particular stations, however, are much improved by including décollement slip. Displacements at stations north of the rift zone are not over-predicted as much as they are with dike-only models (Fig. 14, a). The modeled tilt at KAE is down to the north when including décollement slip, which does not occur in dike-only models (Fig. 14, b). Lastly, modeled GPS displacements at the west flank sites PGF1, PGF5, and PGF6 are oriented to the southeast, consistent with previous slow-slip events (Fig. 14, c).

4. Discussion

We draw two major conclusions from our modeling of the June 17-19, 2007 Kīlauea intrusion and eruption: 1) two *en echelon* dikes provide a much better fit to local surface displacements than curved dike models and 2) décollement slip is required to fit the far-field displacements resulting from this intrusion. The *en echelon* model is consistent with observed locations of surface cracking, steaming areas, and lava, and provides a better fit to surface deformation near the dikes, while including the décollement improves fits to the GPS sites north of the rift and on the western flank as well as coastal tilt.

While the seismic response of Kīlauea's south flank to rift zone intrusions is well known [e.g., *Dvorak et al.*, 1986], this event is the first observed concurrent magmatic intrusion and slow-slip event on Kīlauea [*Brooks et al.*, 2008]. Whether flank sliding is driven by magmatic intrusions or whether intrusions are driven by extensional stress from flank slip is an ongoing discussion. Both processes are likely significant in all intrusions, and many models include interactions between magmatic activity and flank motion. *Dieterich*

[1988] for example, used numerical models to show that a feedback arises between the maximum height that magma can rise within the rift zone, fault friction, and fault width, thereby allowing fault friction to control flank slope. The interaction of the rift zone and décollement during this event suggest that these processes can take place on short time scales. Indeed, *Brooks et al.* [2008] showed the intrusion caused an increase of Coulomb failure stress on the décollement, suggesting that the stress change led to the slow-slip event.

While our preferred model includes two *en echelon* dikes, two Mogi sources, and slip along the basal décollement, exploring simpler model spaces using MCMC methods proved useful in constraining the range of possible source geometries. The bottom depth of $\sim$2 km, similar to those for the January 1997 (Episode 54) and September 1999 intrusions [*Owen et al.*, 2000b; *Cervelli et al.*, 2002a], suggests a change from episodic to continuous deformation at this depth; $\sim$2 km is consistent with the top of the deep rift zone magma body postulated by *Delaney et al.* [1990]. Interestingly, this intrusion also appears to fill a gap between the 1997 and 1999 intrusions (Fig. 15). This gap was the only segment of the middle east rift zone that had not hosted an intrusion since 1983.

While the January 1997, September 1999, and June 2007 dike geometries are similar, we argue that the change from deflation to inflation at Kīlauea's summit in 2003 led to increased magma pressure [*Miklius*, 2005] and hence a more forcible intrusive process. We compare observations of this intrusion to the January 1997 (Episode 54) [*Owen et al.*, 2000b] and September 1999 intrusions/eruptions [*Cervelli et al.*, 2002a], which were also observed by the continuous GPS network and modeled as dikes using similar methods.

We conceptualize Kīlauea's shallow plumbing since 1983 as an open magmatic system consisting of a shallow summit magma chamber connected via a conduit to the ERZ vents similar to *Swanson et al.*'s [1976] model for earlier eruptions. Near simultaneous tilt observations at the summit and Pu'u 'Ō'ō imply that there must be a hydraulic connection between the two [*Cervelli and Miklius*, 2003]. Although this intrusion shares the geometric similarities noted above, this intrusion occurred under different circumstances than the Episode 54 and September 1999 intrusions. The Episode 54 and September 1999 intrusions occurred during persistent post-1983 summit deflation. Lavas from Episode 54 contained a mix of old and new magmas, suggesting that the eruption exploited long lived magma lenses remaining in the rift zone from previous eruptions [*Thornber et al.*, 2003]. Further, Episode 54 was accompanied by limited seismicity localized about the eruptive vent at Nāpau Crater. Based on these observations, *Owen et al.* [2000b] and *Cervelli et al.* [2002a] suggest that the January 1997 and September 1999 intrusions/eruptions were "passive," driven by accumulating rift extension.

In contrast, the 2007 intrusion occurred during a period of inflation which began in 2003 and has been interpreted as resulting from an increase in magma supply to the volcano [*Poland et al.*, 2008]. The June 2007 event was accompanied by more than 180 shallow M>2 earthquakes. While the seismicity pattern of the 1999 intrusion is similar to that of the 2007 intrusion, the 1999 intrusion had fewer total earthquakes and did not reach the surface. Erupted 2007 lava is also more primitive and $30-50^{o}$C hotter than that erupted in 1997, and $\sim15^{o}$C hotter than Episode 55 lava (erupted between 1997 and 2007 from Pu'u 'Ō'ō) [*Thornber et al.*, 2007]. We therefore classify this event as an "active" intrusion, as suggested by *Poland et al.* [2008], implying that it was not entirely driven by passive opening of the ERZ, but was also driven by some component of magma overpressure in the summit reservoir (Fig. 15).

In conclusion, the June 2007 dike event can be well modeled by ∼2 m of opening on a pair of *en echelon* dikes. The concurrent slow-slip event is similar to previous events, and produced ∼15 cm of southward offshore décollement slip. The shallow magmatic system was pressurized during this event, leading to forcible intrusion of the *en echelon* dikes.

Acknowledgments. We would like to acknowledge our collaborators at the University of Hawaii and at the Hawaiian Volcano Observatory. We would like to thank D. Swanson and J.R. Murray for extensive comments on the initial manuscript. Some of the data used in this study was collected using instruments installed as part of an National Science Foundation Small Grant for Exploratory Research, and the work was supported by a National Science Foundation grant. EMB was supported by a National Aeronautics and Space Administration Earth Systems Science graduate fellowship. We would also like to thank K.M. Larson for providing the kinematic GPS solutions.

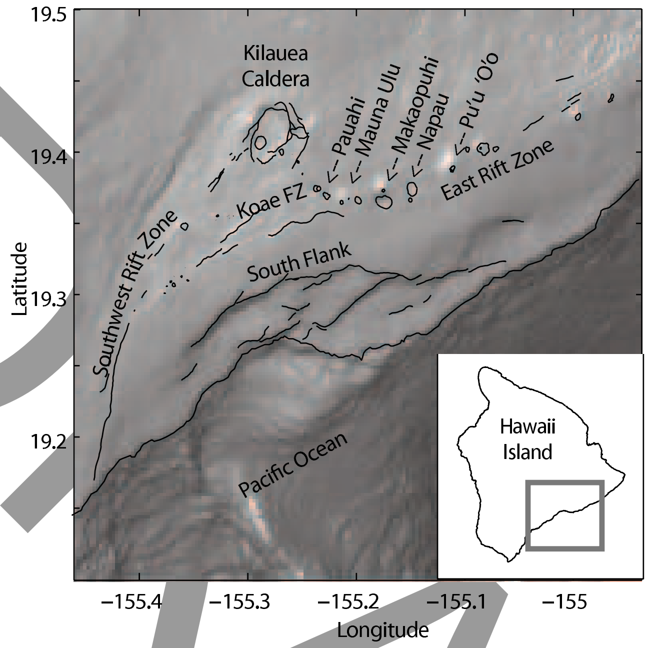

Figure 1. Combined bathymetry and topography of Kīlauea volcano from NOAA data. Major structural features noted in the text are labeled. Inset indicates position of map on the Island of Hawaii.

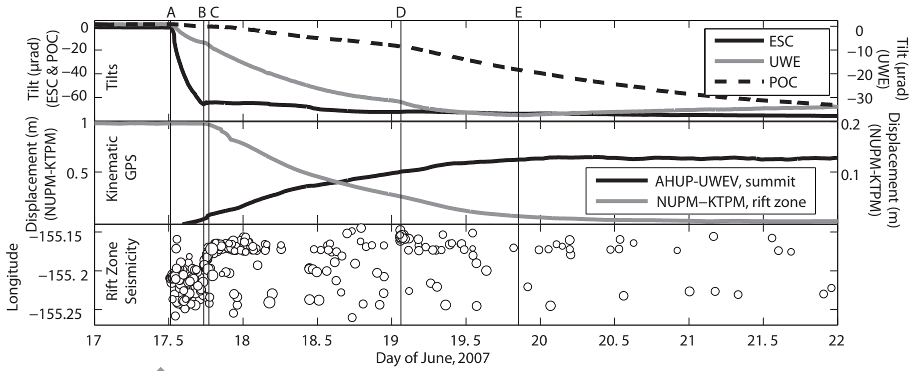

Figure 2. Time history (UTC) of intrusion. **Top**: north component of ERZ (ESC), summit (UWE), and Puʻu ʻŌʻō (POC) tilt. A negative tilt indicates tilt to the south. **Middle**: line length changes between pairs of summit and ERZ GPS stations, kinematically processed for 4 minute positions (note: kinematic data provided by K.M. Larson are presented for reference, but only daily solutions were used in this study). **Bottom**: Catalog locations of rift zone seismicity [*Nakata and Okubo*, 2008]. GPS station and tiltmeter locations are shown in Figures 3 and 4 respectively. Summit GPS displacements and tilts are scaled to aid in comparing event timings; scale factors are noted in the legend of each frame. Vertical bars indicate the following events discussed in the text: **(A)** 12:16 - ESC and UWE tilt begins with onset of seismicity **(B)** 17:40 - ESC tilt flattens, seismicity concentrates down-rift **(C)** 19:00 - seismicity concentrates down-rift, summit tilt rate increases **(D)** 1:15 - slight increase in tilt rate at UWE and down-rift concentration of seismicity **(E)** 20:30 - summit tilt returns to inflation.

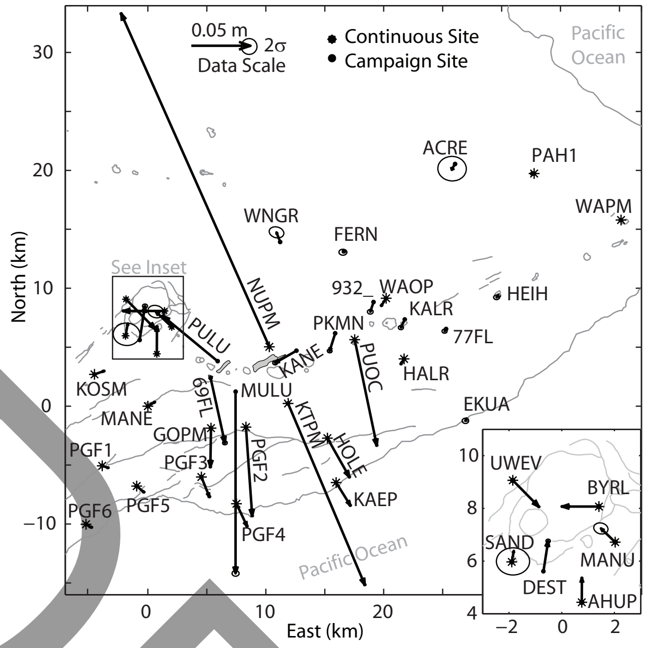

Figure 3. GPS displacements with 95% confidence ellipses. Many ellipses are smaller than the arrowheads. Continuous station locations are marked by an asterisk. Eruption site and steaming areas are outlined in heavy gray (near GPS station PULU, and between NUPM and KTPM). Continuous GPS displacements are calculated for a time period between January 1, 2007 and July 1, 2007 using a least squares inversion for displacements (Eq. 2). Campaign displacements are calculated from the pre- and post- intrusion 2007 campaigns. See text for processing details. The origin of the local Cartesian coordinate system is station MANE (-155.273, 19.339).

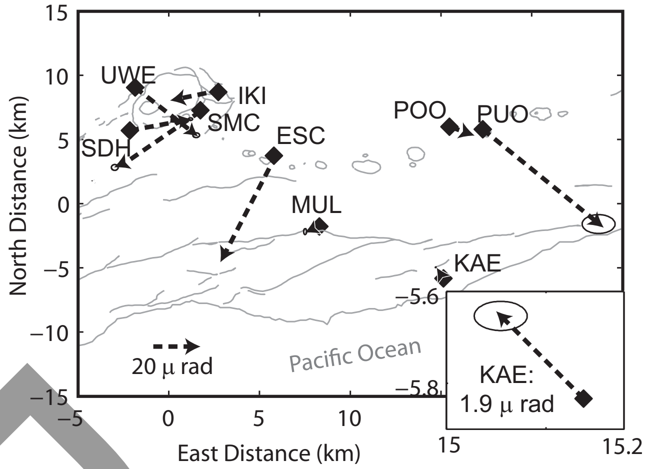

Figure 4. Tilt offsets calculated as the difference in average tilt between June 10-13 and June 22-25. 2σ error ellipses are computed from the standard deviations during both time periods; many ellipses are smaller than the arrowheads.

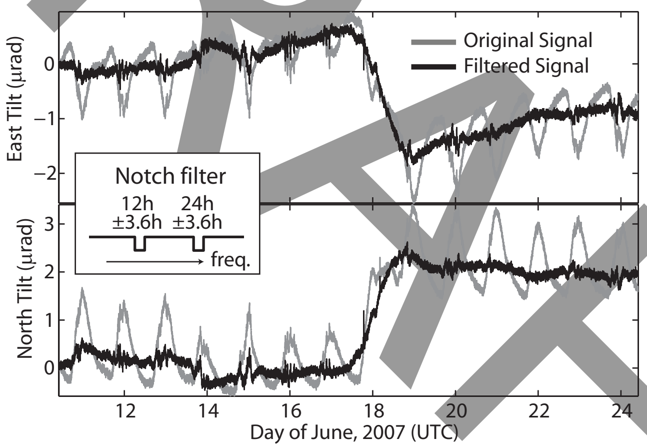

Figure 5. Original east and north components (gray) and notch-filtered output (black) of KAE tilt. Diurnal and tidal frequencies have been removed from the filtered output using notch bandwidths of 3.6 hours.

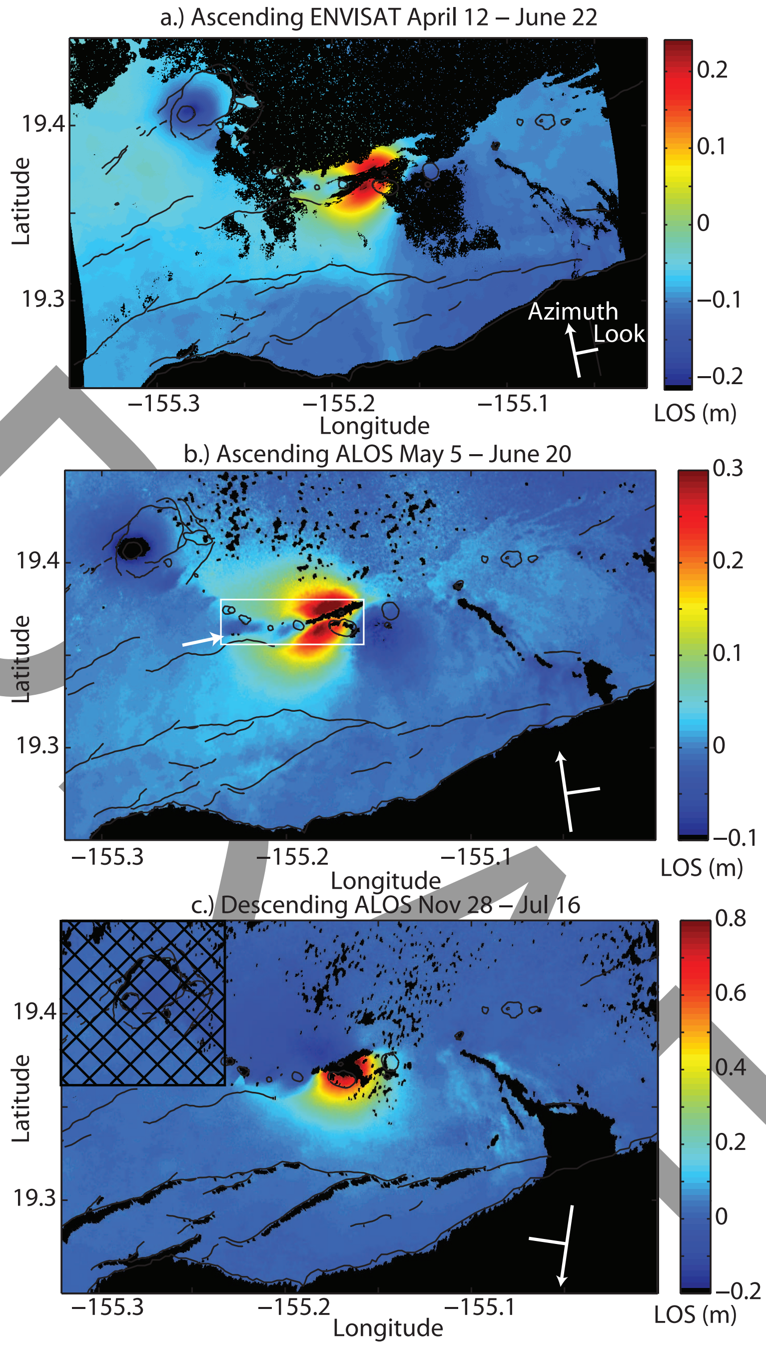

Figure 6. **a.)** ENVISAT ASAR interferogram spanning 12 April - 22 June, 2007. **b.)** ALOS PALSAR ascending image spanning 5 May - 20 June 2007. **c.)** ALOS PALSAR descending interferogram spanning 28 November 2006 - 16 July 2007. All color scales show LOS displacements in meters. The summit area (cross hatched) of the descending ALOS image (**c**) is not used in inversions because of deformation following the intrusion. The white arrow on the ascending ALOS interferogram (**b**) near the bend in the ERZ identifies the discontinuity discussed in the text, while the white box outlines the area shown in Figure 7.

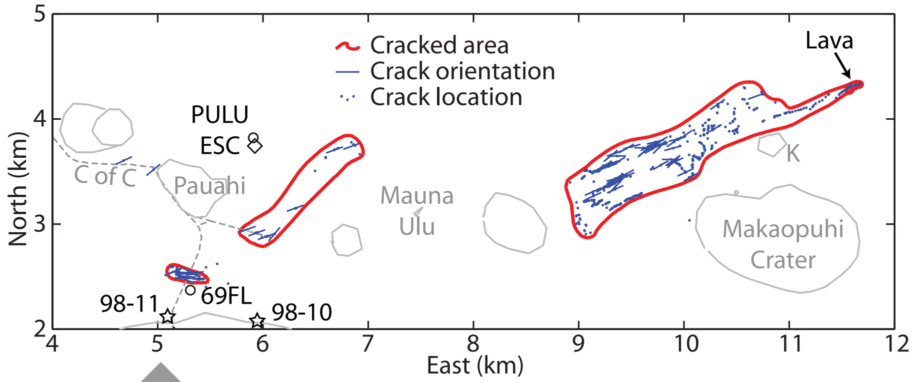

Figure 7. Mapped crack locations (dots) and orientations (small lines). Nearby GPS (PULU and 69FL, marked with circles) and tilt (ESC, marked with a diamond) sites are labeled. PULU and ESC are co-located. Stars mark the location of crack stations 98-10 and 98-11. Just north of Makaopuhi Crater, "K" marks the summit area of Kāne Nui O Hamo lava sheild, on which the farthest eastward extent of the surface cracking and the small lava flow were observed. 'C of C" marks Chain of Craters Road. The road toward Mauna Ulu ends at the Nāpau trail head. The two small craters on either side of Mauna Ulu have been filled by subsequent lava flows.

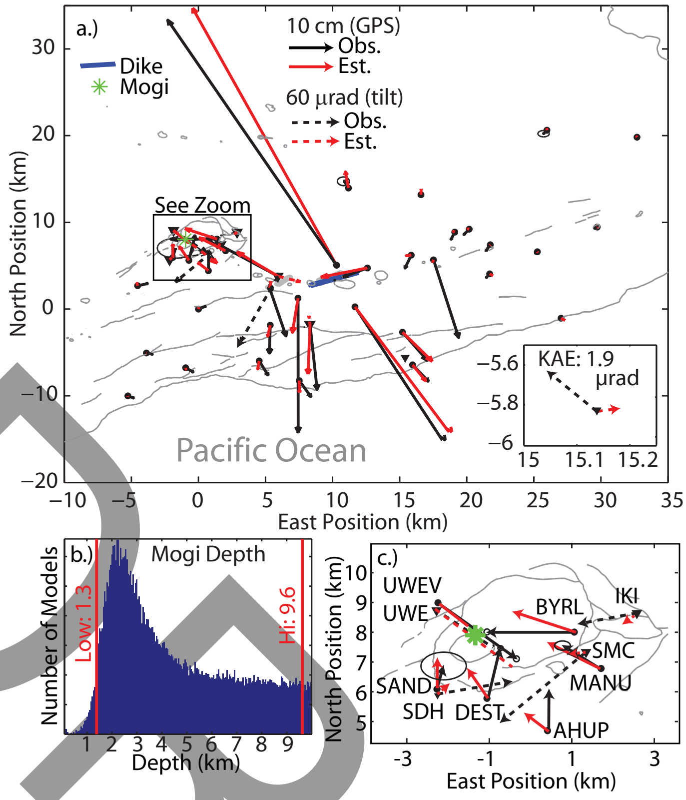

Figure 8. **a.)** Observed (black) and estimated (red) GPS displacements (solid lines) and tilts (dashed lines) from the optimal uniform opening dike model. Lava and steaming areas are outlined in heavy gray, butare partially covered by the dike. **b.)** Posterior distribution of depths to the Mogi source. **c.)** Summit area of the map.

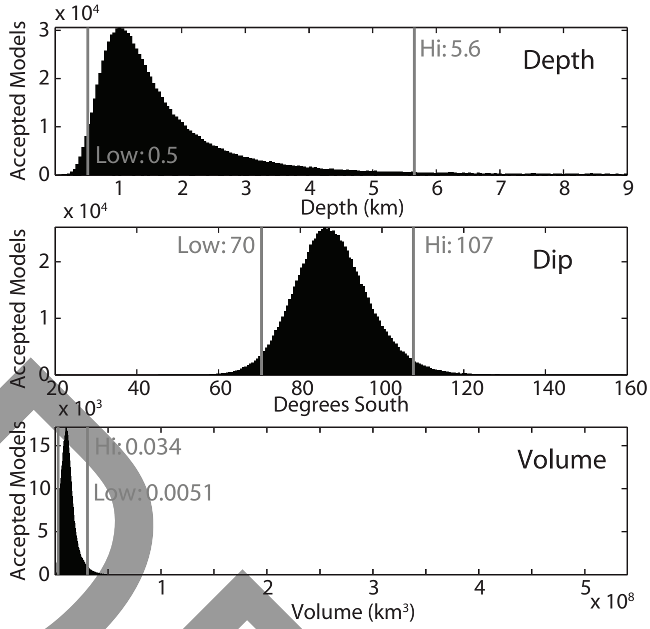

Figure 9. Histograms of depth to the dike bottom, dip, and volume from 1,000,000 Monte Carlo samples of the model space. Vertical bars indicate 95% confidence bounds, while horizontal axis limits are the *a priori* parameter bounds.

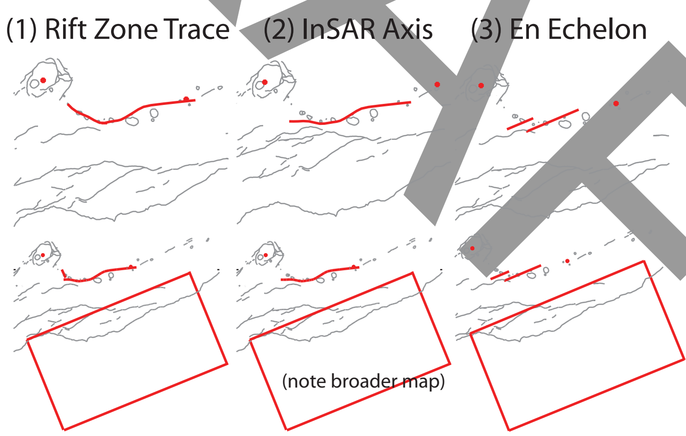

Figure 10. Schematic dike-only models (top) and models including décollement slip (bottom) explored with distributed opening and distributed fault slip. Red dots at the summit and Pu‘u ‘Ō‘ō indicate Mogi source positions.

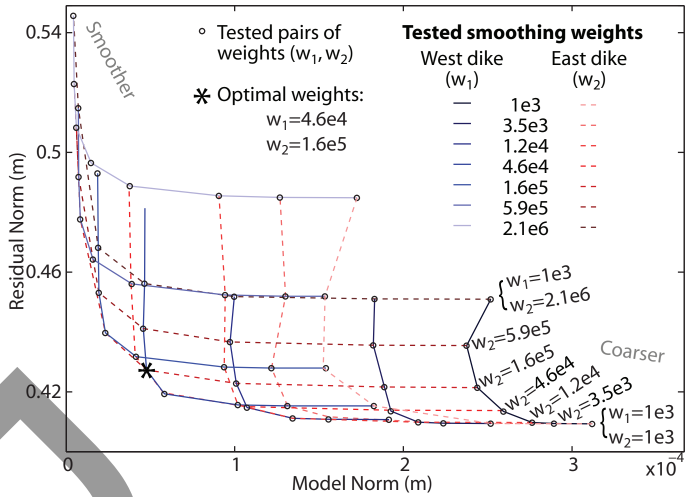

Figure 11. Example L-curves showing the grid search of smoothing parameters for the *en echelon* dike model. Blue solid lines connect tests using the same value of the smoothing parameter on the western segment (w_1), while red dashed lines connect tests using the same smoothing parameter on the eastern segment (w_2). Each dot represents the test of a pair of parameters from which the model norm and residual norm were calculated. The asterisk marks the pair of weights used in the inversion.

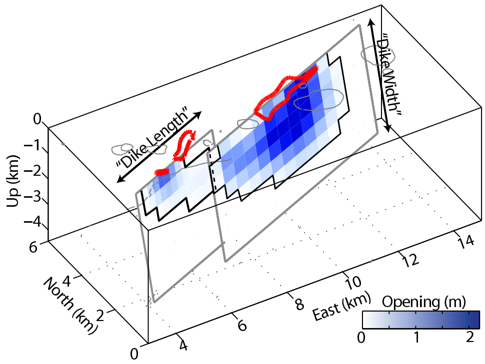

Figure 12. Dike opening distribution from the *en echelon* model. Arrows labeled "dike length" and "dike width" define the model parameters following [*Okada*, 1985]. Gray outlines show the model elements that are allowed to open in inversions, while the black outlines enclose the resulting nonzero opening distribution. The intensity of the blue color indicates the amount of opening on that patch of the dike. Without constraint, most opening is located beneath mapped areas of surface cracking.

Table 1. Percentage of the data variance explained by each type of model.

Model	Dike Only			Dike and Decoll.		
	Rift Zone	InSAR Axis	En Echelon	Rift Zone	InSAR Axis	En Echelon
% Var. Total	0.44	0.88	0.89	0.59	0.78	0.90
% Var. GPS	0.82	0.91	0.89	0.85	0.94	0.92
% Var. Tilt	0.62	0.61	0.85	0.55	0.62	0.83
% Var. SAR	0.42	0.88	0.90	0.57	0.78	0.89

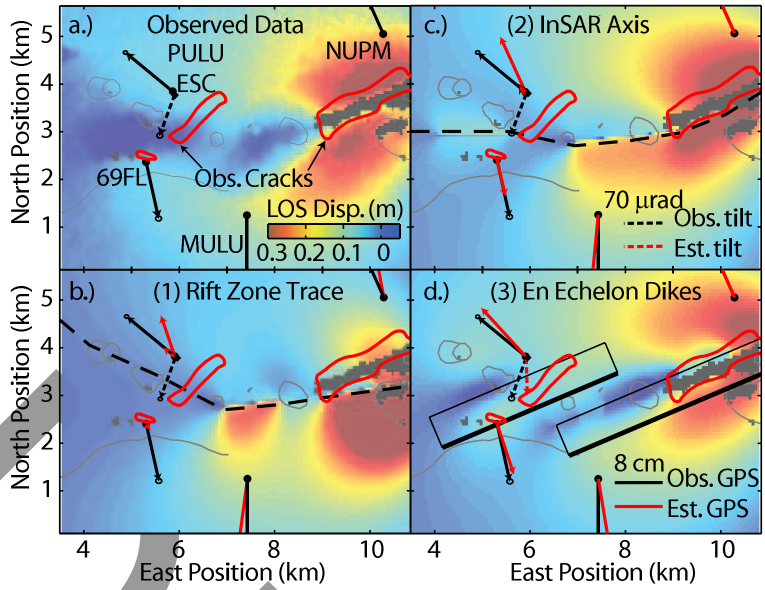

Figure 13. A comparison of model predictions for each of the dike-only models, focused on the near-field deformation. **a.)** Observed data; **b.)** Model (1) following the surface trace of the rift zone (51%) ; **c.)** Model (2) following the symmetry axis of the InSAR data (89% of InSAR variance explained by this model); **d.)** Model (3), a pair of *en echelon* dikes (89%). The $\sim 110^o$ difference in displacement and tilt directions at co-located GPS site PULU and tilt site ESC are not able to be replicated by curving dike models following either the surface trace of the rift zone or the symmetry axis of the InSAR data.

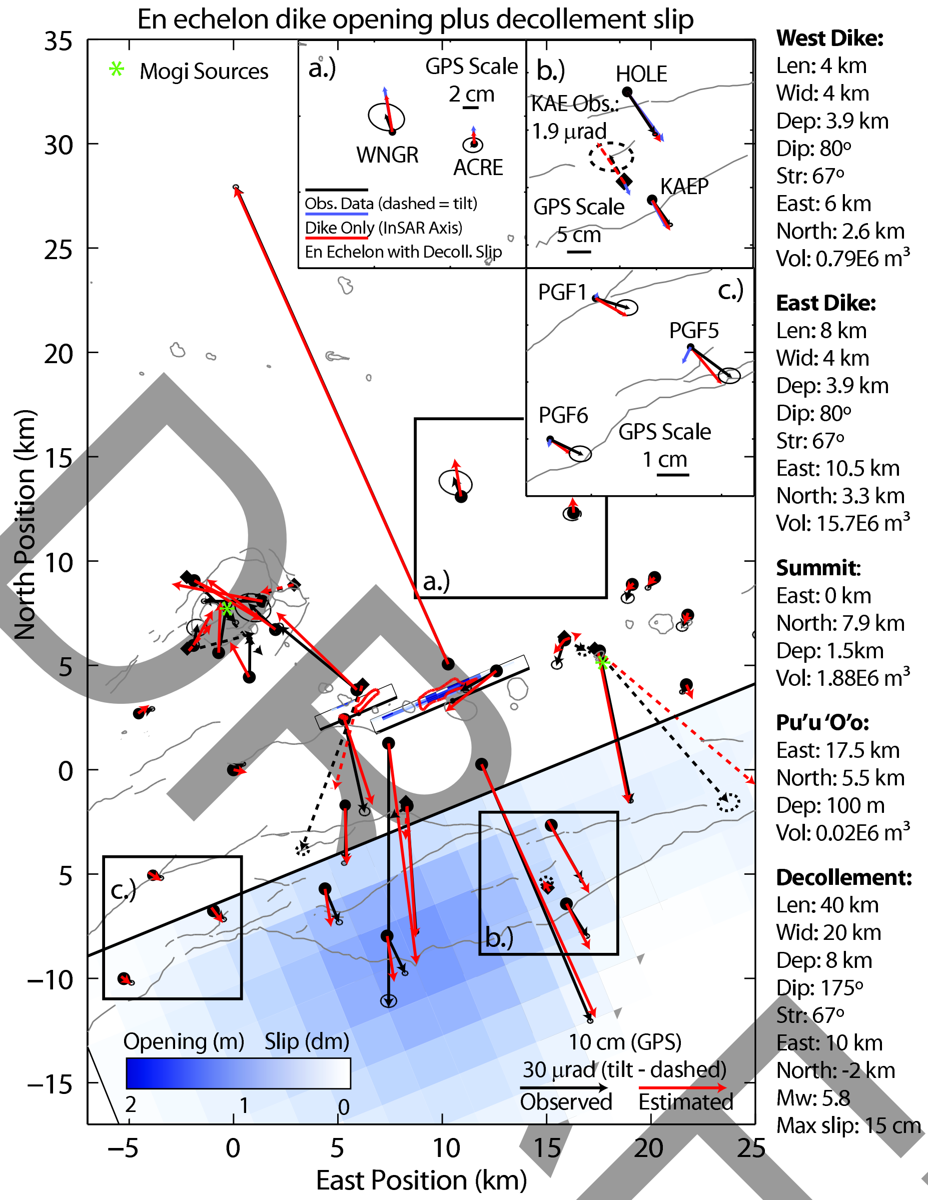

Figure 14. Preferred model of the deformation associated with the June 17-19 intrusion including two *en echelon* dike segments and décollement slip. Dislocation model parameters represent the full extent of allowed opening in inversions, and are measured from the center of the bottom edge, with length measured along strike and width along dip, which is nearly vertical. Volumes are computed by integrating the distributed opening model, in which many patches, especially deeper patches, have zero opening (see Fig. 12). Boxes indicate detail insets. Detail views emphasize local improvements over dike-only models after adding décollement slip: **a.)** North flank GPS displacements, **b.)** coastal site KAE, and **c.)** displacements at southwestern flank sites.

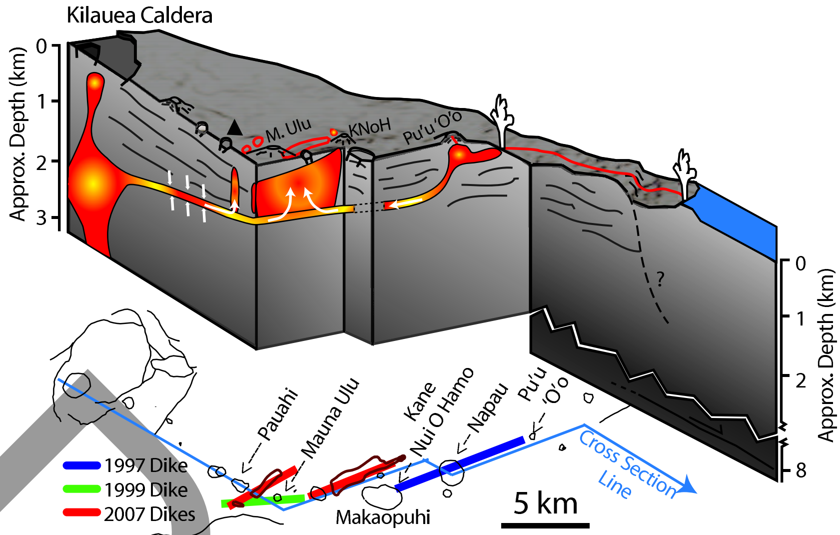

Figure 15. Schematic cross section of Kīlauea's shallow plumbing system and the intrusive process [*Johnson*, 2000]. Map view shown below also identifies the locations of the 1997 and 1999 intrusions.

References

516 Altamimi, Z., X. Collilieux, J. Legrand, B. Garayt, and C. Boucher (2007), Itrf2005: A new release of the international terrestrial reference frame based on time series of station positions and earth orientation parameters, *J. Geophys. Res.*, *112*, B09,401, doi:doi:10.1029/2007JB004949.

519 Brooks, B., J. Foster, D. Sandwell, C. Wolfe, P. Okubo, M. Poland, and D. Myer (2008), Magmatically triggered slow slip at kilauea volcano, hawaii., *Science*, *321*(5893), 1177, doi: 10.1126/science.1159007.

522 Brooks, B. A., J. H. Foster, M. Bevis, L. N. Frazer, C. J. Wolfe, and M. Behn (2006), Periodic slow earthquakes on the flank of kilauea volcano, hawai'i., *Earth and Planetary Science Letters*, *246*(3/4), 207 – 16, doi:10.1016/j.epsl.2006.03.035.

Cervelli, P., and A. Miklius (2003), The shallow magmatic system of Kilauea Volcano, *USGS Prof. Paper 1676*, pp. 149 – 163.

Cervelli, P., P. Segall, F. Amelung, H. Garbeil, C. Meertens, S. Owen, A. Miklius, and M. Lisowski (2002a), The 12 September 1999 Upper East Rift Zone dike intrusion at Kilauea Volcano, Hawaii - art. no. 2150, *J. Geophys. Res.*, *107*(B7), 2150 – 2150, doi:10.1029/2001JB000602.

Cervelli, P., P. Segall, K. Johnson, M. Lisowski, and A. Miklius (2002b), Sudden aseismic fault slip on the south flank of Kilauea volcano, *Nature*, *415*(6875), 1014 – 1018.

Delaney, P., R. Fiske, A. Miklius, A. Okamura, and M. Sako (1990), Deep Magma Body Beneath the Summit and Rift Zones of Kilauea Volcano, Hawaii, *Science*, *247*(4948), 1311–1316.

Dieterich, J. (1988), Growth and persistence of Hawaiian volcanic rift zones, *J. Geophys. Res.*, *93*(B5), 4258–4270.

Dvorak, J., A. Okamura, T. English, R. Koyanagi, J. Nakita, M. Sako, W. Tanigawa, and K. Yamashita (1986), Mechanical response of the south flank of Kilauea Volcano, Hawaii, to intrusive events along the rift systems., *Tectonophysics*, *124*(3/4), 193 – 209.

Dvorak, J. J., and D. Dzurisin (1997), Volcano geodesy: the search for magma reservoirs and the formation of eruptive vents., *Reviews of Geophysics*, *35*(3), 343 – 84, doi:10.1029/97RG00070.

Edmonds, M., and T. Gerlach (2007), Vapor segregation and loss in basaltic melts, *Geology*, *35*(8), 751.

Fiske, R., and R. Koyanagi (1968), The December 1965 Eruption of Kilauea Volcano, Hawaii, *U.S. Geological Survey Professional Paper 607*, pp. 1–22.

Fukuda, J., and K. Johnson (2008), A Fully Bayesian Inversion for Spatial Distribution of Fault Slip with Objective Smoothing, *Bulletin of the Seismological Society of America*, *98*(3), 1128.

Got, J.-L., and P. Okubo (2003), New insights into Kilauea's volcano dynamics brought by large scale relative relocation of microearthquakes., *J. Geophys. Res.*, *108*(B7), 2337 – 2350, doi:10.1029/2002JB002060.

Gregorius, T. (1996), *GIPSY-OASIS II: How it Works*, (self-published), Univ. of Newcastle upon Tyne, New Castle, England, U.K.

Gudmundsson, A. (2003), Surface stresses associated with arrested dykes in rift zones, *Bulletin of Volcanology*, *65*(8), 606–619.

Hansen, P. (1992), Analysis of discrete ill-posed problems by means of the l-curve, *SIAM Review*, *34*(4), 561–580.

Hansen, S., C. Thurber, M. Mandernach, F. Haslinger, and C. Doran (2004), Seismic velocity and attenuation structure of the east rift zone and south flank of Kilauea Volcano, Hawaii., *Bulletin of the Seismological Society of America*, *94*(4), 1430 – 40.

Heliker, C., and T. Mattox (2003), The first two decades of the pu'u o'o–kupianaha eruption: chronology and selected bibliography, *USGS Prof. Paper 1676*, pp. 1–28.

Johnson, J. (2000), Diagram of kilauea, Website.

Metropolis, N., A. Rosenbluth, M. Rosenbluth, A. Teller, and E. Teller (1953), Equation of state calculations by fast computing machines, *Journal of Chemical Physics*, *21*, 1087 – 1092.

Miklius, A. (2005), Recent Inflation of Kilauea Volcano During the Ongoing Eruption-Harbinger of Change?, *American Geophysical Union, Fall Meeting 2005, abstract# G53B-0883*, *86*(52).

Miklius, A., P. Cervelli, M. Sako, M. Lisowski, S. Owen, P. Segal, J. Foster, K. Kamibayashi, and B. Brooks (2005), Global positioning system measurements on the island of hawai'i: 1997 through 2004, *USGS Open File Report 2005-1425*, pp. 1–48.

Miyazaki, S., J. McGuire, and P. Segall (2003), A transient subduction zone slip episode in southwest Japan observed by the nationwide GPS array, *J. Geophys. Res.*, *108*(B2), 2087 – 2087, doi:10.1029/2001JB000456.

Mogi, K. (1958), Relations between the eruptions of various volcanoes and the deformations of the ground surfaces around them, *Bull. Earthquak Res. Inst. Univ. Tokyo*, *36*, 111–123.

Montgomery-Brown, E., D. Sinnett, P. Segall, A. Miklius, M. Poland, and K. Larson (2007), Source models of the June 17, 2007 intrusion at Kilauea volcano, Hawaii: Spatio-temporal evolution, *EOS, Trans., AGU Fall Meet. Suppl.*, *88*(52), abstract V52A-1138.

Montgomery-Brown, E., P. Segall, A. Miklius, P. Cervelli, and D. Shelly (2009), Slow slip events on kilauea volcano, hawai'i, *Journal of Geophysical Research*, in Press.

Morgan, J., and P. McGovern (2003), Discrete element simulations of volcanic spreading: implications for the structure of Olympus Mons, *Lunar and Planetary Science XXXIV*, abstract 2088.

Nakamura, K. (1980), Why do long rift zones develop in Hawaiian volcanoes–A possible role of thick oceanic sediments., *Bull. Volcanol. Soc. Japan*, *25*, 255–267, in Japanese.

Nakata, J., and P. Okubo (2008), Hawaiian volcano observatory seismic data, january to december, 2007, *USGS Open File Report 2008-1261*, pp. 1–99.

Okada, Y. (1985), Surface deformation due to shear and tensile faults in a half-space, *Bull. Seismol. Soc. Am.*, *75*, 1135–1154.

Owen, S., P. Segall, M. Lisowski, A. Miklius, R. Denlinger, and M. Sako (2000a), Rapid deformation of Kilauea Volcano: Global positioning system measurements between 1990 and 1996, *J. Geophys. Res.*, *105*(B8), 18,983 – 18,998.

Owen, S., P. Segall, M. Lisowski, A. Miklius, M. Murray, M. Bevis, and J. Foster (2000b), January 30, 1997 eruptive event on Kilauea Volcano, Hawaii, as monitored by continuous GPS, *Geophys. Res. Letters*, *27*(17), 2757 – 2760.

Poland, M., A. Miklius, T. Orr, A. J. Sutton, C. Thornber, and D. Wilson (2008), New episodes of volcanism at kilauea volcano, hawaii, *EOS Trans. AGU*, *89*(5), 37–48.

Rivalta, E., and P. Segall (2008), Magma compressibility and the missing source for some dike intrusions, *Geophys. Res. Lett*, *35*.

Segall, P., E. Desmarais, D. Shelly, A. Miklius, and P. Cervelli (2006), Earthquakes triggered by silent slip events on Kilauea Volcano, Hawaii, *Nature*, *442*, doi:10.1038/nature04938.

Swanson, D. A., W. A. Duffield, and R. S. Fiske (1976), Displacement of the south flank of Kilauea Volcano, Hawaii: The result of forceful intrusion of magma into the rift zones, *USGS Prof. Paper 963*, pp. 1–39.

Thornber, C., T. Orr, H. Lowers, C. Heliker, and R. Hoblitt (2007), An Episode 56 Perspective on Post-2001 Comagmatic Mixing Along Kilauea's East Rift Zone, *American Geophysical Union, Fall Meeting 2007, abstract# V51H-04*.

Thornber, C. R., et al. (2003), Kilauea east rift zone magmatism: An Episode 54 perspective, *J. of Petrology*, *44*(9), 1525 – 1559.

Welstead, S. T. (1999), *Fractal and wavelet image compression techniques,*, 232 pp., SPIE Optical Engineering Press, Bellingham, Washington.

Wilson, D., J. Uribe, S. Kamibayashi, J. Nakata, and P. Okubo (2007), Seismic Characterization of the June 17, 2007 East Rift Intrusion at Kilauea Volcano, *American Geophysical Union, Fall Meeting 2007, abstract# V51H-02*.

Wolfe, C., B. Brooks, J. Foster, and P. Okubo (2007), Microearthquake streaks and seismicity triggered by slow earthquakes on the mobile south flank of Kilauea Volcano, Hawai'i, *Geophys. Res. Lett*, *34*, doi:10.1029/2007GL031625.

Zumberge, J. F., M. B. Heflin, D. C. Jefferson, M. M. Watkins, and F. H. Webb (1997), Precise point positioning for the efficient and robust analysis of GPS data from large networks., *Journal of Geophysical Research*, *102*(B3), 5005 – 17.